BIOHYBRID ROBOTS

Remote control of muscle-driven miniature robots with battery-free wireless optoelectronics

Yongdeok Kim[1,2]†, Yiyuan Yang[3,4]†, Xiaotian Zhang[5]†, Zhengwei Li[6,7,8]†, Abraham Vázquez-Guardado[6]†, Insu Park[2], Jiaojiao Wang[2,9], Andrew I. Efimov[10], Zhi Dou[5], Yue Wang[6,10], Junehu Park[1], Haiwen Luan[6], Xinchen Ni[6], Yun Seong Kim[5], Janice Baek[1,2], Joshua Jaehyung Park[3], Zhaoqian Xie[11], Hangbo Zhao[12], Mattia Gazzola[5,13,14]*, John A. Rogers[3,6,10,15,16,17]*, Rashid Bashir[1,2,5,9,14,18]*

Bioengineering approaches that combine living cellular components with three-dimensional scaffolds to generate motion can be used to develop a new generation of miniature robots. Integrating on-board electronics and remote control in these biological machines will enable various applications across engineering, biology, and medicine. Here, we present hybrid bioelectronic robots equipped with battery-free and microinorganic light-emitting diodes for wireless control and real-time communication. Centimeter-scale walking robots were computationally designed and optimized to host on-board optoelectronics with independent stimulation of multiple optogenetic skeletal muscles, achieving remote command of walking, turning, plowing, and transport functions both at individual and collective levels. This work paves the way toward a class of biohybrid machines able to combine biological actuation and sensing with on-board computing.

INTRODUCTION

Biohybrid systems consisting of living and artificial components that recapitulate biological architectures and functions can enhance our understanding of biological systems and foster new applications in implantable devices (*1*), regenerative medicine (*1*), organs-on-a-chip (*2*, *3*), and soft robotics (*4*–*15*). Recently, biohybrid robots consisting of cells and soft materials have demonstrated the ability to sense, respond, and adapt to environmental cues in real time (*4*), achieving life-like functions such as swimming, walking, and pumping (*5*–*15*). Demonstrations range from biohybrid rays (*5*) and fish (*6*) based on sheets of optogenetic cardiomyocytes and neuromuscular junction–driven microswimmers (*7*) to walkers, grippers, swimmers, and pumps that use three-dimensional (3D) skeletal muscle tissue (*8*–*13*) activated either electrically or by light.

Although collectively these prototypes offer a variety of solutions aimed at improving performance and controllability, limitations persist in terms of coordination of advanced functionalities. Some of these systems rely on electric stimulations that require electrodes to invasively penetrate or contact tissue. This method is also poorly selective because electricity will pass through tissue and medium and activate cells regardless of type. Optogenetics, which is a biological technique that exploits light to activate transgenic cells, has provided a powerful paradigm to enable noninvasive and localized stimulation within biohybrid robots (*5*–*8*). Nonetheless, optogenetic-based control requires light sources placed near the muscles of interest and high intensities to activate transfected opsins, rendering manually directed light stimulation—the only approach demonstrated so far—cumbersome and of limited applicability.

In this regard, the integration of on-board lightweight, miniaturized, and flexible electronics to command and power multiple light points distributed at precise locations, without the hindering motion, becomes an attractive option. The integration of bioelectronics has great potential for robotic functions demonstrated by recent advances in neuromodulation and sensing in vivo (*16*–*20*) as well as electrical modulation or recording of muscle actuations of a tethered, nonmotile system in vitro (*2*, *3*, *13*, *14*). Here, we present a wirelessly controlled biohybrid electronic robot (eBiobot) driven by a battery-free optoelectronic device with wireless communications, allowing remote control of switching, steering, and other more sophisticated functions (Fig. 1A and Movie 1). The eBiobot inherits the structural concept motivated by a physiological muscle-tendon-bone architecture from previously demonstrated walking robots (*8*–*10*), where 3D-engineered skeletal muscle tissue forms around an asymmetric hydrogel scaffold. Responding to external stimuli, muscles perform cyclic contractions, deform the

[1]Department of Materials Science and Engineering, University of Illinois at Urbana-Champaign, Urbana, IL 61801, USA. [2]Nick J. Holonyak Micro and Nanotechnology Laboratory, University of Illinois at Urbana-Champaign, Urbana, IL 61801, USA. [3]Department of Mechanical Engineering, Northwestern University, Evanston, IL 60208, USA. [4]Department of Mechanical Engineering, Massachusetts Institute of Technology, Cambridge, MA 02139, USA. [5]Department of Mechanical Science and Engineering, University of Illinois at Urbana-Champaign, Urbana, IL 61801, USA. [6]Querrey Simpson Institute for Bioelectronics, Northwestern University, Evanston, IL 60208, USA. [7]Department of Biomedical Engineering, University of Houston, Houston, TX 77204, USA. [8]Department of Biomedical Sciences, University of Houston, Houston, TX 77204, USA. [9]Department of Bioengineering, University of Illinois at Urbana-Champaign, Urbana, IL 61801, USA. [10]Department of Biomedical Engineering, Northwestern University, Evanston, IL 60208, USA. [11]State Key Laboratory of Structural Analysis for Industrial Equipment, Department of Engineering Mechanics, DUT-BSU Joint Institute, Dalian University of Technology, Dalian 116024, China. [12]Department of Aerospace and Mechanical Engineering, University of Southern California, Los Angeles, CA 90089, USA. [13]National Center for Supercomputing Applications, University of Illinois at Urbana-Champaign, Urbana, IL 61801, USA. [14]Carl R. Woese Institute for Genomic Biology, University of Illinois at Urbana-Champaign, Urbana, IL 61801, USA. [15]Department of Electrical and Computer Engineering, Northwestern University, Evanston, IL 60208, USA. [16]Department of Materials Science and Engineering, Northwestern University, Evanston, IL 60208, USA. [17]Department of Neurological Surgery, Feinberg School of Medicine, Northwestern University, Chicago, IL 60611, USA. [18]Department of Electrical and Computer Engineering, University of Illinois at Urbana-Champaign, Urbana, IL 61801, USA.
*Corresponding author. Email: rbashir@illinois.edu (R.B.); jrogers@northwestern.edu (J.A.R.); mgazzola@illinois.edu (M.G.)
†These authors contributed equally to this work.

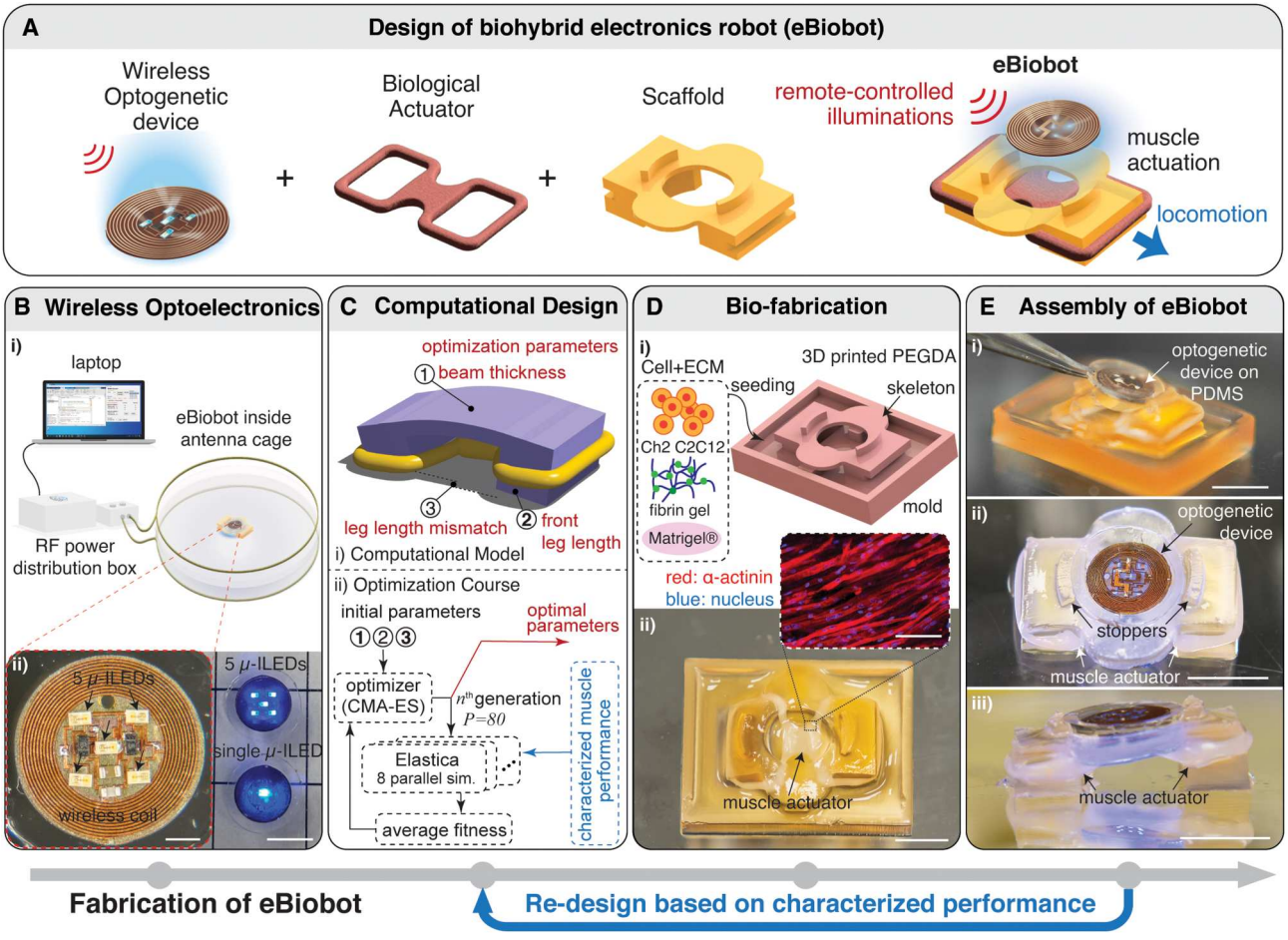

Fig. 1. Schematic and workflow for fabrication and optimization of the single actuator eBiobot. (**A**) Schematic of key components of eBiobot and its design goal. (**B**) Experimental setup and the wireless optogenetic control system. Schematics for (i) experimental setup of wireless communications with the battery-free optogenetic device using μ-ILEDs as local stimulation sources and (ii) photographic images of the optogenetic device with a single (bottom) and five μ-ILEDs (top). Left inset is the expanded view of a five μ-ILED device. (**C**) Computational design optimization. (i) Computational model using Elastica. The scaffold is constructed by two legs with length mismatch connected with a thin, connecting beam. (ii) Optimization course. Three key scaffold characteristics were selected as design parameters for optimization (**D**) Biofabrication of eBiobot. (i) Schematics of the fabrication for engineered skeletal muscle tissue actuator integrated with 3D-printed hydrogel by seeding optogenetic transfected myoblasts and extracellular matrix mixture. (ii) Photographic image of eBiobot with muscle actuator wrapping around 3D-printed skeleton inside the mold. Inset shows the fluorescence image of muscle actuator. Red, α-actinin; blue, DAPI. (**E**) Modular assembly of eBiobot. (i) Assembling wireless optogenetic device onto the skeleton using tweezers and (ii) angled and (iii) side-view photographic images of assembled eBiobot after releasing from the mold. Scale bars, 5 mm [Bii (right), Dii, and E (i, ii, and iii)], 1 mm [inset of (Bii)], and 100 μm [inset of (Dii)].

scaffold, and propel the robot through asymmetric friction generated at the scaffold-substrate interface.

RESULTS

The battery-free, wireless optogenetic devices exploited resonant magnetic induction between paired transmission (at the circumference of the experimental enclosure) and a receiving (at the perimeter of the device) antenna system operating at radio frequency (RF; 13.56 MHz) to power microinorganic light-emitting diodes (μ-ILEDs) to actuate the optogenetic muscles (Fig. 1B and figs. S1 to S5). Amplitude modulation of the RF power produced on-off patterns of operation at programmable frequencies and pulse widths relevant for the optical stimulation of eBiobots contained within the experimental antenna cage, with a diameter of 15 cm (Fig. 1Bi). Constituent layers for the wireless electronic module

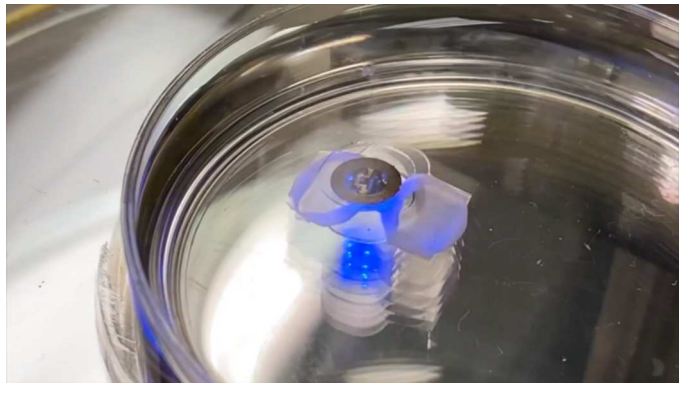

Movie 1. Overview of the wirelessly controlled biohybrid electronic robot (eBiobot).

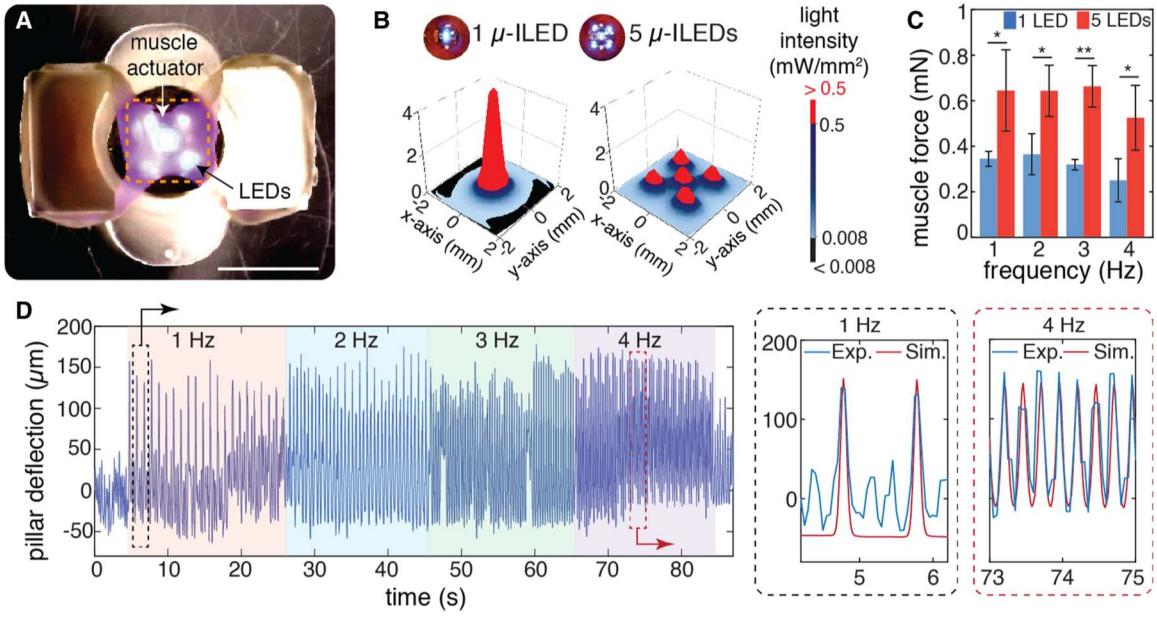

Fig. 2. Characterization of muscle performance in the eBiobot stimulated by wireless controlled μ-ILEDs. (**A**) Optical image of the eBiobot shining with five μ-ILEDs. (**B**) Light intensity on the surface of a muscle actuator in the region of orange dotted square in (A) when stimulated by one μ-ILED and five μ-ILEDs. Red area in (B) indicates higher light intensity for saturated force, and black region indicates lower light intensity for threshold of optogenetics muscle to activate, resulting in a contraction (*3*, *30*). (**C**) Muscle active forces stimulated by one μ-ILED (blue bar graphs) and five μ-ILEDs (red bar graphs) with different frequencies. *P < 0.05 and **P < 0.01. Error bars correspond to the SDs from three measurements from three different samples. (**D**) Pillar deflection curves stimulated by five μ-ILEDs at different frequencies. Insets show the comparison with simulations. Scale bar, 5 mm.

included a thin double-sided flexible circuit board composed of rolled annealed copper layers (18 μm) separated by a polyimide film (75 μm) and a conformal encapsulation layer of parylene (about 14 μm) to isolate the device from the cell culture medium (fig. S2). This encapsulation strategy has been proven to protect devices for over 80 days in saline solution and for over 60 days after in vivo implantation in rodents (*17*, *21*). Five μ-ILEDs electrically connected in parallel and distributed at the center and inner corners produced the illumination spatial profile to trigger muscle contractions (Fig. 1Bii). Overall device flexibility, lightweight construction (about 7.3 mg), wireless power transfer, and control capability enabled robust real-time remote operation of eBiobots.

Although on-board optoelectronics provided the ability to command individual muscles, the overall walking performance of the eBiobot was determined by a complex interaction between active forces of muscle contraction and passive tension (*9*, *10*), electronic component integration, interfacial mechanics, and fluid drag (fig. S6). Therefore, quantitative identification and optimization of robust designs were crucial. Here, we demonstrated and optimized the eBiobot design and functionality through an iterative design approach that involved multiple stages of evolutionary design optimization, fabrication, and testing (Fig. 1, C to E). We started off by computationally modeling the biohybrid walker as a heterogeneous assembly of slender elastic, passive (scaffold), and active (muscles) elements. To this end, we used the solver Elastica (fig. S6), a Cosserat rod solver that has been extensively validated and demonstrated in a variety of biophysical settings, including biohybrid robotics (*22*, *23*). The geometric characteristics of beam thickness, front leg length, and leg length mismatch were numerically identified as key to the eBiobot's walking abilities (Fig. 1Ci). We then coupled Elastica with an evolutionary algorithm (*24*) to optimize these parameters for fast-forward speed. The optimization process accounted for variations in biological muscle characteristics and actuation, ensuring robust performance of the final design (Fig. 1Cii; details on the optimization process are provided in Materials and Methods).

The design blueprint was then materialized through biofabrication and additive manufacturing, where an in vitro engineered skeletal muscle tissue formed around a 3D-printed hydrogel scaffold (Fig. 1D and figs. S7 and S8). The centimeter-scale (1.4 cm by 0.7 cm) scaffold was designed to hold the optogenetic device (5 mm in diameter) in the center (fig. S7). The eBiobot was then deployed in the antenna arena to test its mobility and controllability (Fig. 1E). To systematically improve the eBiobot's performance, we characterized the variation of muscle forces in each batch of the experiment, feeding that information into the next design iteration.

A challenge in achieving locomotion is to effectively stimulate the optogenetic muscles so as to generate sufficiently strong contractions using μ-ILEDs as localized illumination sources. Our designs addressed this challenge in the following ways, as demonstrated in Fig. 2. First, the 3D-printed mold was designed to match the shape of the muscle tissue with the spatial arrangement of μ-ILEDs (Fig. 2A, fig. S7, and movie S1). Second, we distributed five μ-ILEDs at the center and corners of a circle as defined by the inner radius of the receiver antenna. This design choice maximized the illumination area at the center of the muscle actuator (Fig. 2, A and B) where the muscular forces are produced to deflect the scaffold. Even though the cost of a μ-ILED's individual illumination intensity (details of illuminations of one and five μ-ILEDs in fig. S9, A to C) was lower, the final design was found to

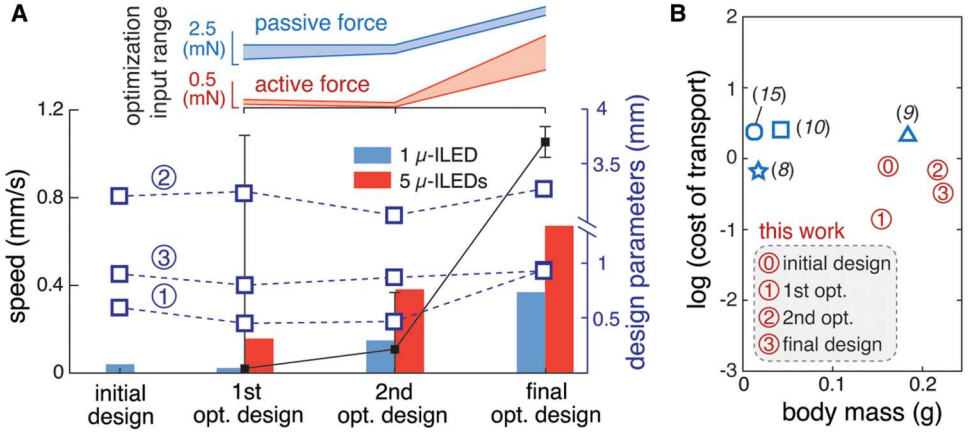

Fig. 3. Design iterations for the eBiobot. (**A**) Each optimization incorporates muscle force sampled from the given input range. For the first optimization iteration, this range was obtained by experimentally characterizing the passive and active muscle forces in the initial design. Subsequently, force characterized from each optimized design was used to set the range for the next iteration. Mean walking speed from the simulation was compared with experimental results stimulated by one or five μ-ILEDs. Error bars indicate the magnitude of SD normalized to the mean speed. Three design parameters are plotted for each optimization iteration with (i) beam thickness, (ii) front leg length, and (iii) leg length mismatch. (**B**) Efficiency analysis through COT. Designs from all iterations are compared against previous biohybrid walkers (*8*–*10*, *15*).

induce larger muscle contraction forces across a range of stimulation frequencies in Fig. 2C and figs. S9, D and E, and S10. Muscle actuators showed contractile properties and durability over 2 to 3 weeks after differentiation after the use of the antifibrinolytic agent to inhibit the secretion of proteases (*25*, *26*).

After establishing the integration of μ-ILEDs and muscles, we fabricated a proof-of-concept single-actuator unidirectional eBiobot prototype to characterize and validate our computational model. The performance was found (movie S2) to be in good agreement with the observed deformation of the eBiobot legs across a range of actuation frequencies (Fig. 2D). With this model, we then set out to optimize the walking performance of the eBiobot.

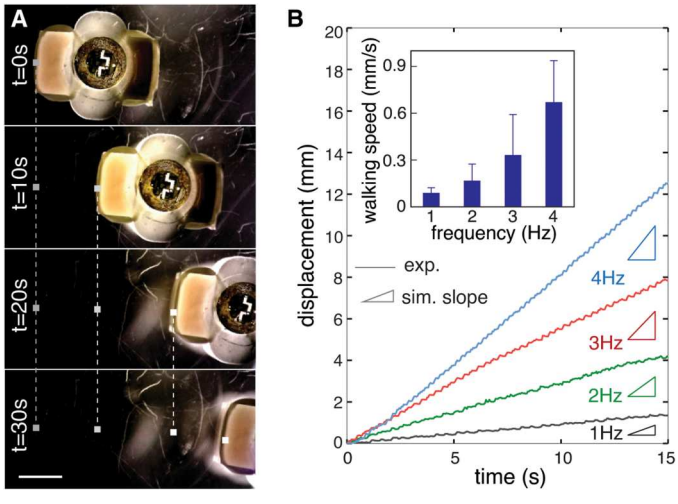

Fig. 4. Walking performance of the eBiobot equipped with five μ-ILEDs and driven with 10-W RF power. (**A**) Time-lapse images of eBiobot from the last design iteration stimulated at 4 Hz. (**B**) Time-dependent displacement of the eBiobot at different stimulation frequencies. Inset shows the average speed. Error bars correspond to the SDs from three measurements from three different samples. Scale bar, 5 mm.

In each optimization campaign, hundreds of different scaffolds were generated and numerically evaluated using muscle forces sampled from the experimentally characterized range (Fig. 3A). Subsequently, an optimal design was obtained with geometric characteristics resulting in the fastest walking speed given the specific force range (Fig. 3A; full details of the design iterations can be found in fig. S11). The obtained optimal solution was fabricated, characterized, and tested. The newly acquired muscle responses were aggregated to the initial set, thus improving our data-driven muscle model in concert with the evolution of the scaffold design. Over three campaigns, speed was improved by a factor of 10 relative to our initial design (Fig. 3A, figs. S11 and S12, table S1, and movie S3). We also noted that, relative to previous biohybrid walker examples, our eBiobot exhibits comparable efficiency as evaluated through cost of transport (COT) (Fig. 3B), defined as the muscle output energy needed to transport the walker for a certain distance (full description can be found in Materials and Methods).

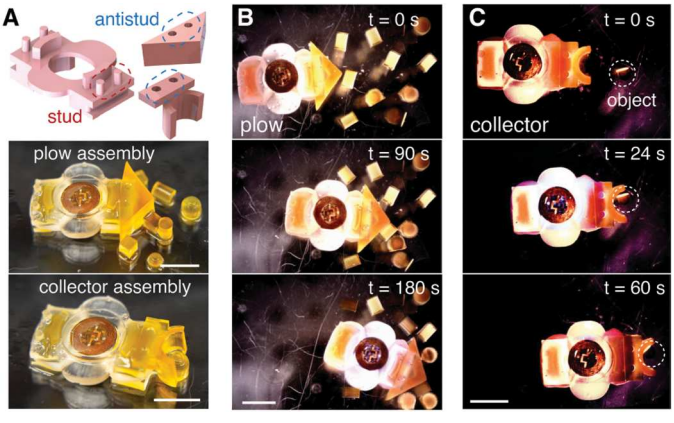

Fig. 5. Robotic functionality of eBiobot. (**A**) Schematics of LEGO block assembly with skeleton. Images of plow and collector assemblies. Time-lapse images of (**B**) plow-attached eBiobot displacing objects and (**C**) collector-attached eBiobot transporting an object. Scale bars, 5 mm.

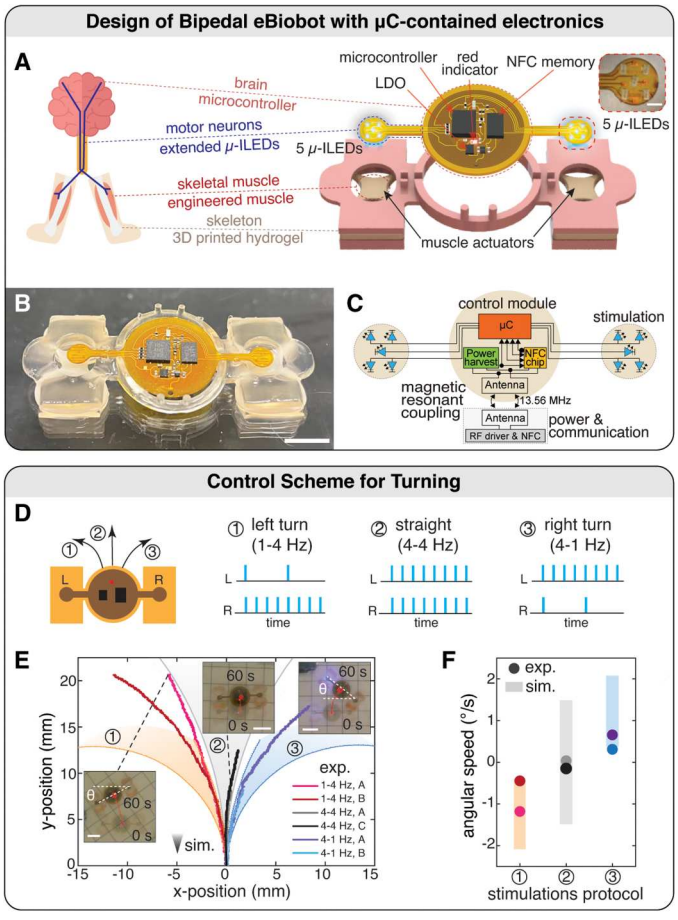

Fig. 6. Bipedal eBiobot can be controlled to turn in different directions. (**A** to **C**) Bioinspired design and μC-containing electronics for bipedal eBiobot. (A) Schematic of biological motor unit–inspired design and μC-containing electronics with components for bipedal walking. Inset shows the image of five μ-ILEDs. (B) A prototype of the assembled bipedal robot. (C) Block diagrams of the μC-containing wireless electronic control system. The system contains a μC that reads and operates the stimulation parameters updated in an NFC memory chip in real time. (**D** to **F**) Control scheme for turning. (D) Schematic of bipedal eBiobot and optical stimulations with its turning directions. (E) Trajectories and (F) angular speeds stimulated by dual panels μ-ILEDs with (i) 1 and 4 Hz, (ii) 4 and 4 Hz, and (iii) 4 and 1 Hz for left and right sides in 60 s. The computational turning scopes were obtained by considering muscle force variations. Scale bars, 1 mm [inset of (A)] and 1 cm (others).

The walking performance of the final eBiobot design is further characterized in Fig. 4A. A maximum walking speed of 0.83 mm/s was achieved when the eBiobot was stimulated at 4 Hz, 50-ms pulse width, and 10-W RF antenna power (movie S4), setting a speed record among skeletal muscle–based biohybrid robots (table S2). This speed was attributed to the combination of applied frequencies, optimized spatial μ-ILED arrangement, and surface friction. First, we noted that walking speeds increase with applied frequencies, as illustrated in the linear displacement-time curves of Fig. 4B and movie S5, corroborating computational predictions. Second, the use of five μ-ILEDs was found to provide wider illumination, favorable muscle contractions (as previously discussed in Fig. 2, B and C), and faster walking speed (fig. S13 and movie S6). In addition, on the basis of the confocal image analysis of the muscle actuator (figs. S14 to S17 and movie S7), the rotation angle and arrangement of five μ-ILEDs were optimized to match the myotube alignment. Last, surface friction was also optimized by exploring different substrate chemistries because the walking speed depends on the friction coefficient (fig. S18) (*15*, *27*).

In addition to walking, robotic functionality was demonstrated using accessory tool attachments inspired by the LEGO block assembly (Fig. 5). A 3D-printed accessory such as a plow or collector was plugged on a pair of pillars at the top of the scaffold, with stud and antistud coupling, allowing the user to switch tools on a skeleton for specific applications (Fig. 5A and fig. S19). In the first demonstration, a plow attached to the eBiobot was able to move scattered objects (Fig. 5B and movie S8). In a second demonstration, a collector was attached to the robot and shown to be capable of picking up and moving objects (Fig. 5C and movie S9).

In a step toward enhanced maneuverability, a second eBiobot inspired by bipedal architecture and biological motor units (Fig. 6) was designed to have two muscle actuators in combination with a central microcontroller (μC), which extends laterally to bring two circular plates that hold five μ-ILEDs in intimate proximity with the muscle actuators (Fig. 6, A and B, and figs. S20 to S22). The connection part in the center of the bipedal eBiobot skeleton held the μC-containing wireless optogenetic device. Both front and rear legs contact the surface on which the eBiobot crawls, as can be seen in fig. S22 (F and G). The combination of standardized near-field communication (NFC) protocols, low-power electronics, and μC with specialized firmware allowed for the implementation of wireless real-time control on illumination parameters (frequencies and pulse widths) and illumination profiles delivered to any arbitrary combination of μ-ILEDs (Fig. 6C and fig. S23). This bipedal eBiobot system implements locomotion manipulation by enabling individual and localized control of contractions at different locations of the muscles within the same biohybrid robot. Furthermore, the use of NFC chipsets allowed us to target individual devices to implement multiunit coordinated control among eBiobot clusters.

We numerically modeled this bipedal eBiobot to predict its motion characteristics under different stimulation protocols, whereby muscles can be either symmetrically (both 4 Hz) or differentially (4 and 1 Hz) stimulated (Fig. 6D). To ensure robustness across locomotion modes, we did not set muscle forces to be constant values but instead sampled from the range characterized during the final optimization iteration (737 to 1403 μN; Fig. 3A). As shown in Fig. 6E, by symmetric or differential stimulation of both muscles, the in silico bipedal eBiobot exhibited robust forward and bidirectional steering motions (movie S10 and fig. S24). The optimized friction coefficient (fig. S18) was included in our computational model during our design to reveal the traction force of the walker at the leg-substrate interface that ultimately determines and explains the motion of the bot (fig. S25). This design was realized in experiments, successfully demonstrating the predicted locomotion modes under user-programmable remote control (Fig. 6, E and F; fig. S26; and movies S11 and S12). To further highlight the eBiobot's ability to maneuver, we challenged it to traverse an obstacle course. Figure 7 (A and B) shows a clockwise half turn through obstacles over a duration of about 9.5 min, under 4 and 1 Hz of stimulation on left and right legs, respectively (movie S13). Moreover, by swapping the stimulation frequencies on both legs, we demonstrated in Fig. 7 (C and D) its capability of bidirectional turning in one continuous run controlled using a wireless remote control (movie S14

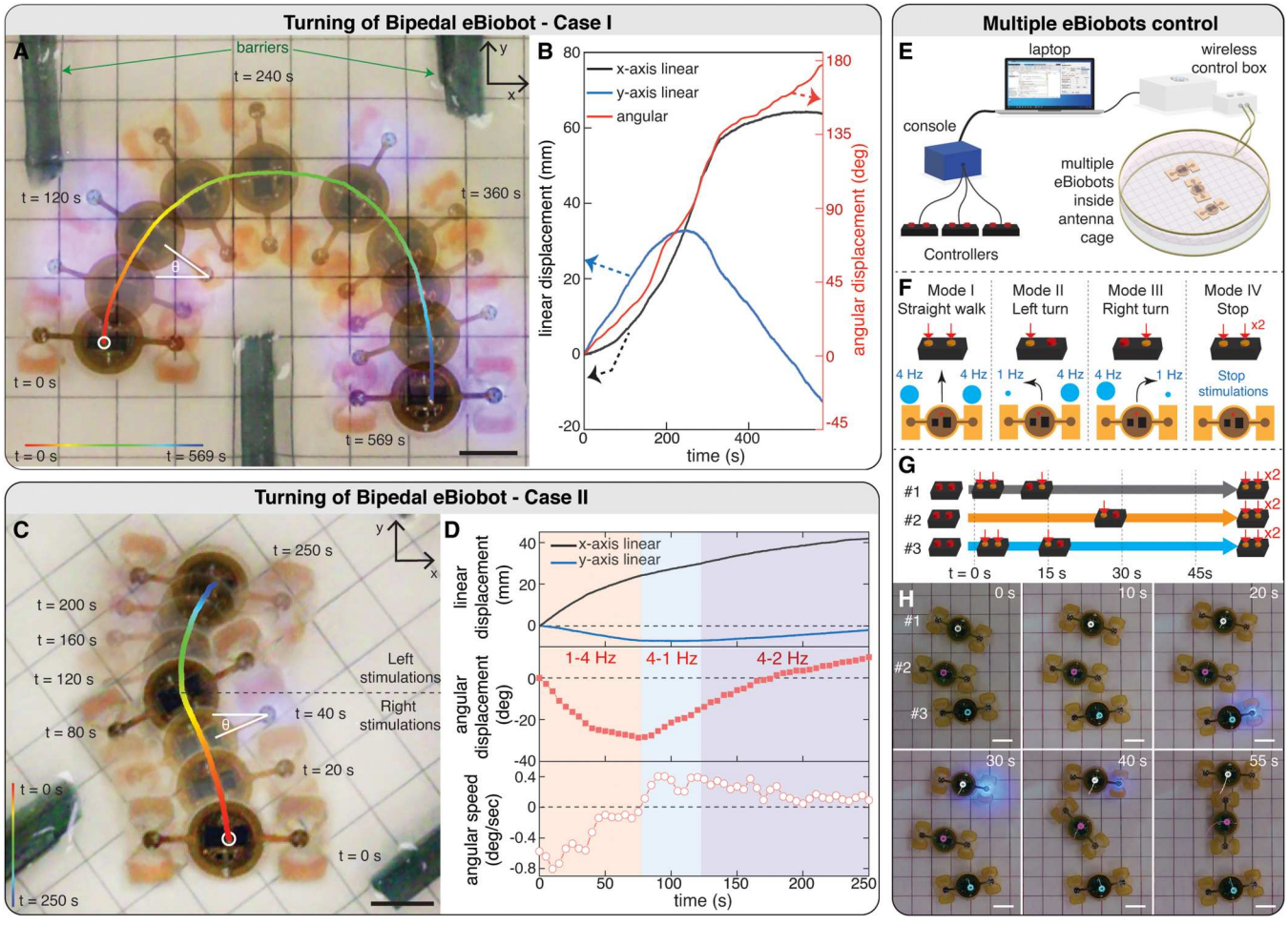

Fig. 7. Turning of bipedal eBiobot and control of multiple robots. (**A** and **B**) Turning bipedal robot through barriers. (A) Trajectory and time-lapse images of the turning eBiobot (in 569 s). Color map shows the elapsed time. (B) Linear and angular displacements with time. (**C** and **D**) Bidirectional turning of the bipedal eBiobot. (C) Trajectory and time-lapse images of bidirectional-turning eBiobot (in 250 s). Color map shows the elapsed time. (D) Linear and angular displacements as well as angular speed with time and stimulation. (**E** to **H**) Controlling multiple robots using a console system. (E) Experimental setup for individual remote-controlled multiple bipedal eBiobots using a console system connected with multiple gaming controllers. (F) Operation modes of clickers to start, turn and stop bipedal robots corresponding with their stimulations. Manipulation of three robots. (G) Operation modes of gaming controllers for the three eBiobots with time. (H) Time-lapse images over 55 s for the corresponding trajectories of the three eBiobots. Scale bars, 1 cm.

and fig. S27). Furthermore, we illustrated a console system connected with multiple gaming controllers for the individual manipulation of a multitude of eBiobots, with each controller used for one eBiobot (Fig. 7E and figs. S28 and S29). The on-board μ-ILED panels were activated according to a preset stimulation pattern, assigned to clicker buttons on a joypad (Fig. 7F and movie S15), through our customized software (fig. S29). Three bipedal eBiobots were then manipulated by three gaming controllers to make an "I" (Fig. 7, G and H, movie S16, and fig. S30).

DISCUSSION

In this work, we present biohybrid electronic robots powered by optogenetic skeletal muscles and controlled by wireless optoelectronics. The robot architecture and locomotion performance were computationally optimized through a staged iterative process, incorporating fabrication and experimental testing for robustness. The eBiobots were designed and fabricated to bring together three different classes of components: the biological muscle tissue actuator, electronic components such as μ-ILEDs and the wireless electronics, and the 3D-printed hydrogel skeleton. These three components with contrasting mechanical properties were designed and optimized while physically assembling them together to result in the integrated functional system. A range of functionalities and capabilities can be expanded along each of the component types. Our designs, along with 3D printing additive manufacturing, allowed for seamless integration of on-board electronics, multiple muscle actuators, and LEGO-like structures and attachments. The device platform and design approach allowed for programmable functionalities such as remote control switching, steering, plowing, and transportation of objects, both for individual robots and multiple robots that could be individually controlled. For example, different muscle types could be used to expand functionality, as well as the use of different opsins resulting in control with

different wavelengths (*6*). The onboard electronics could include sensing, memory, storage, and closed-loop control toward autonomous functions. We also demonstrated precise local stimulation of the optogenetic skeletal muscle cells using the integrated μ-ILEDs as compared with stimulation from a distance, thus allowing for control of multiple muscle actuators on the same device and enabling for 2D walking and steering of the eBiobots. The speed of the device was eventually limited by the active tension produced by the muscle tissue and the mechanical design of the scaffold (*8*–*10*). The iterative modeling and simulation approach was used to optimize the physical parameters of the scaffold, resulting in a 10× increase in the speed of the robots (*10*, *22*, *23*). The operation of the muscle tissues requires a glucose-rich fluid environment at 37°C. However, future use of cells from other organisms such as insects could potentially enable room temperature operation. Although the molecular weight of the hydrogels can be designed to produce a specific mechanical modulus and the hydrogel can be 3D-printed to produce a desired shape, the hydrogel scaffolds required hydration to maintain their printed form and the mechanical properties to produce the desired functional response upon the muscle actuation.

In conclusion, the building blocks demonstrated here could be used to design higher-order structures and systems that could combine the advantages of living tissues, 3D-printed additive manufacturing, and optoelectronics and pave the way for biohybrid miniature robots with integrated electronics and multicellular engineered living systems for a wide range of potential applications.

MATERIALS AND METHODS

Fabrication process for wireless optogenetic devices

A trilayer stack Cu (18 μm)/polyimide (75 μm)/Cu (18 μm) (Pyralux AP8535R, DuPont) served as the fabrication substrate for the flexible printed circuit board (fPCB). Laser ablation process (ProtoLaser U4, LPKF Laser & Electronics) defined the layout of the device, including receiver coil, circuits, and soldering pads. The components were mounted and soldered on the fPCB using low-temperature tin-bismuth-silver alloy solder paste (ChipQuik) and hot air soldering processing. Last, chemical vapor deposition (Specialty Coating Systems) formed a conformal waterproof parylene coating (14 μm) that encapsulated the devices. In this paper, we designed two device configurations: one with passive operation and the other with NFC active operation. For the passive operation, we used either one μ-ILED or five μ-ILEDs electrically connected in parallel and distributed at the center and inner corners to satisfy the illumination requirements. For active operation, we designed a device with two bilateral pads, each containing five μ-ILEDs. These active devices contained an RF-accessible memory (M24LR04E, STMicroelectronics) and a low-power 8-bit μC (Attiny84, Atmel) to implement remote control of the μ-ILED arrays in two modes of operation: (i) synchronous and (ii) asynchronous operation, both with user-programmable frequency and pulse widths.

Design and fabrications of 3D-printed hydrogel

A digital light processing 3D printer (PICO2, Asiga) was used to fabricate hydrogel parts designed in SolidWorks. The printing resin solution was composed of 20% (v/v) of polyethylene glycol diacrylate (molecular weight, 700 g/mol; Sigma-Aldrich) in distilled water containing lithium phenyl-2,4,6-trimethylbenzoylphosphinate (1 mg/ml; Sigma-Aldrich) as a photoinitiator and sunset yellow dye (0.4 mg/ml; Sigma-Aldrich) for the printing resolution by decreasing light scattering effect (*10*). The fabricated structures were soaked in 10% (v/v) of bleach for 30 min to remove the dye from 3D-printed structures, followed by sterilization in 70% (v/v) of isopropyl alcohol overnight and rinsing with phosphate-buffered saline (PBS) in 4°C for at least 4 days before tissue seeding.

Cell culture and tissue fabrications

Optogenetic C2C12 myoblasts (catalog no. CRL-1772, American Type Culture Collection) transfected with blue light–sensitive ion channel channelrhodopsin-2 tagged with tdTomato, namely, ChR2 (H134R), were cultured in the growth medium composed of Dulbecco's modified Eagle medium (DMEM) (Corning) with 10% (v/v) of fetal bovine serum (Lonza), 1% (v/v) of L-glutamine (Corning), and 1% (v/v) of penicillin-streptomycin (Lonza). Five million cells/ml of ChR2 C2C12s were seeded in a 3D-printed mold after mixing with 30% (v/v) of Matrigel (Corning), fibrinogen (4 mg/ml; Sigma-Aldrich), and thrombin (Sigma-Aldrich) with fibrinogen (0.5 U/mg of fibrinogen) (*28*). In the first and second generations of eBiobots, the cell/gel solution was seeded on 3D-printed mold in fig. S12C. In the third and fourth generations of eBiobots and bipedal eBiobots, it was seeded on an assembled structure with skeleton and mold shown in Fig. 1Ci and figs. S7 and S20. The growth medium containing aminocaproic acid (1 mg/ml; Sigma-Aldrich) was added to the seeded tissues with 3D-printed structures after 90 min of seeding, followed by 3 days of incubation for the compaction of cell/gel mixture with the same medium in 37°C. Three days after seeding, the medium was switched into the differentiation medium, DMEM containing 10% (v/v) of horse serum (Thermo Fisher Scientific), 1% (v/v) of penicillin/streptomycin, 1% (v/v) of L-glutamine, aminocaproic acid (1 mg/ml), and insulin-like growth factor-1 (1 ng/ml; Sigma-Aldrich) to differentiate myoblasts to myotubes in muscle actuator.

Integration of battery-free wireless optogenetic devices with eBiobot

In the first and second generations of eBiobots, the wireless optogenetic device with μ-ILEDs as localized stimulators was attached on the 3D-printed stage inside of the skeleton beam as indicated by the red arrows in fig. S12 (A and B). Kwik-Sil Adhesive (World Precision Instruments) was applied on the stage to glue with the backside of the wireless optogenetic device. Then, the muscle actuator was transferred from the mold in fig. S12C on day 9 after differentiation using tweezers. Figure S12 (D and E) shows the wireless optogenetic device on the stage of the beam located between the muscle actuator and skeleton beam. In the third and fourth generations, the wireless optogenetic devices were attached to a circular shape of polydimethylsiloxane (PDMS) (8 mm in diameter) using Kwik-Sil Adhesive before assembling the device/PDMS on the hole of skeleton beam as indicated by the red arrows in fig. S12 (F and G). Stoppers were added on the skeleton in the fourth generation to fit with and hold the device/PDMS stably. A wireless optogenetic device with two separate pads of μ-ILEDs was plugged in and out of the 3D-printed central stage of the bipedal skeleton structure without using adhesive. All electronics and PDMS parts were sterilized with ultraviolet for at least 30 min before and after integrating with eBiobots.

Experimental implementation for wireless communication with the optogenetic devices

The power distribution box (PDB; Neurolux), in conjunction with an RF impedance matching for efficient power transmission and communication (Neurolux), drove a double parallel loop antenna with a 4.8-cm vertical distance that wrapped around the 15-cm–diameter circular container for wireless power transmission to the battery-free wireless optogenetic devices at 13.56 MHz. To operate passive devices (single eBiobot device), we configured the PDB with an RF switch to deliver target operational pulses (for example, 1-Hz pulses for 200-ms pulse widths) to the devices within the experimental arena. To operate active devices (bipedal eBiobot device), we used a customized graphic user interface (GUI) implemented in MATLAB (MathWorks Inc.) to establish communication with the devices via ISO (International Organization for Standardization) 15693 NFC protocol supported by the PDB. This implementation together with the specialized firmware in the μC allowed us to control the operation modality of each individual device such as on/off, synchronous/asynchronous operation, and frequency/pulse width reconfiguration in real time. For the measurement of eBiobots, DMEM without phenol red (Corning) was used to prevent light absorption induced by phenol red.

Immunostaining and fluorescence imaging

Muscle tissues (see "Cell culture and tissue fabrications" section) were removed from the skeletons, rinsed with PBS, and fixed in 4% (v/v) of paraformaldehyde (Electron Microscopy Sciences) for 20 min at room temperature. For cryosectioning of tissues, fixed samples were treated sequentially with sucrose solutions [10, 20, and 30% (w/v)] for 30 min at room temperature. After an overnight incubation with 30% (w/v) of sucrose solution in 4°C and washing with PBS, tissues were embedded in optimal cutting temperature (OCT) resin solution (Tissue-Tek) and snap-frozen on dry ice before storage at −80°C. Frozen tissue molds were sectioned with 50 μm in thickness onto silane-treated glass slides (Electron Microscopy Sciences) using the cryostat (CM3050S, Leica). Sectioned tissue slices were rinsed with PBS to wash out OCT after 1-hour thawing of OCT at room temperature. Samples were bordered with water repellent barrier using Pap pen (Abcam) and blocked with 1% (w/v) of bovine serum albumin (Sigma-Aldrich) in PBS containing 0.1% of Tween 20 detergent (PBST) at 4°C overnight. The primary antibodies, mouse anti-myosin heavy chain, MF-20 (catalog no. 14-6503-82, Thermo Fisher Scientific), and rabbit anti α-actinin (catalog no. ab137346, Abcam) were diluted with a 1:400 ratio in PBST and incubated with tissue samples overnight at 4°C. After washing with PBS three times, the secondary antibodies, Alexa Fluor 488 anti-mouse and Alexa Four 647 anti-rabbit (Thermo Fisher Scientific) with a 1:500 dilution ratio in PBST, were added to stain MF-20 and α-actinin antibodies, respectively, followed by incubation overnight with a 1:5000 dilution ratio of 4′,6-diamidino-2-phenylindole (DAPI) to stain the nucleus at 4°C. After washing with PBS three times for at least 5 min, samples were mounted after adding the VECTASHIELD Antifade Mounting Medium (Vector Laboratories) under a sealed coverslip. The Multiphoton Confocal Microscope Zeiss 710 was used for confocal fluorescence imaging.

Muscle force characterizations and locomotion analysis

Muscle actuation was recorded by the Dino-lite digital microscope camera (Dino-Lite) after flipping the eBiobot over to make the pillars face the camera. Images were acquired at a rate of 20 frames/s. Muscle forces were calculated using the Euler-Bernoulli beam-bending theory (*8*–*10*, *28*, *29*)

$$F = \frac{8EI\delta}{L^2 l}$$

where I is the moment of inertia, δ is the deflection on beam, L is the length of the skeleton beam, and l is the moment arm from the point of applied force of the actuator to the beam. E represents the Young′s modulus of skeleton beam, which was measured to be 270 kPa. The Cannon EOS Rebel T5i was used for recording of walking and turning for bipedal eBiobots at a rate of 29.87 frames/s. The movement of pillars and locomotion of eBiobots were tracked using the software Tracker (https://physlets.org/tracker). The white circles on the electronics in Fig. 7 (A and C) are the tracking points for the trajectory color map. The angular displacements and speed in Fig. 7 (B and D) were analyzed on the basis of the orientations of the device arm in Fig. 7 (A and C). The linear and angular displacements in fig. S30 were analyzed on the basis of the tracking points in circles for eBiobot 1, 2, and 3 in Fig. 7H. Samples were measured between days 15 and 21 after differentiation for force characterizations and locomotion analysis.

Computational modeling of eBiobot

The eBiobot was computationally modeled using solver Elastica, following a similar approach that has been developed and leveraged for modeling biohybrid robots (*7*, *9*, *10*, *23*). Elastica is an open-source software package for simulating assemblies of soft slender bodies using Cosserat rod theory. Cosserat rod is a mathematical description that captures the 3D dynamics of 1D slender bodies while accounting for all modes of deformation (bending, twisting, stretching, and shearing; fig. S6, A to C). The eBiobot was then modeled as an assembly of Cosserat rods specialized to represent the muscle tissues and the scaffold (fig. S6D). This assembly of rods was constructed via appropriate boundary conditions to account for structural connectivity and dynamic interactions among rods. We also took into account the dynamic effects induced by the on-board microelectronics by combining their masses into the rod representing the scaffold. Furthermore, environmental effects such as gravity, buoyancy, surface friction, and hydrodynamics were also characterized and implemented in simulation. Further details relative to our computational approach can be found in Supplementary Methods. The numerical solver Elastica is publicly available at www.cosseratrods.org.

Evolutionary design optimizations

With a computational eBiobot model in hand, we then tackled the problem of optimizing the scaffold to maximize its forward walking speed. To do this, we coupled Elastica with the Covariance Matrix Adaptation Evolution Strategy algorithm (CMA-ES) (*24*), a method specialized for dealing with nonlinear, nonconvex continuous optimization problems. Coupled with Elastica, CMA-ES was demonstrated as an efficient design tool for a range of engineering and biohybrid applications (*22*, *23*).

A critical aspect of designing biohybrid systems in particular was that the characteristics of the biological actuator cannot always be

precisely predicated and controlled. Therefore, an optimal solution obtained by assuming a specified actuation may fail when the actuator performs differently. Here, to overcome this issue, our optimization process of the eBiobot took into account the uncertainties due to the biological muscle variations. The process flow of the optimization course is presented in fig. S11A. We first identified three key scaffold parameters (beam thickness, front leg length, and leg length mismatch) that are most influential on the walking speed and manually picked initial values of these parameters as the input of CMA-ES. For instance, the leg length mismatch for the final eBiobot design was 0.93 mm (long leg length, 3.74 mm; short leg length, 2.81 mm; fig. S7). Then, the CMA-ES evolved these parameters over a number of generations to improve the speed of the bot. In each generation, CMA-ES deploys N (N = 50 to 80) parallel Elastica simulations, with each simulation taking a unique design parameter triple-sampled from a multivariate Gaussian distribution. To evaluate the robustness of each scaffold design, every Elastica simulation created eight exact eBiobots and simulated each one with a different muscle force sampled from the experimentally characterized range. The resulting speeds (defined as the fitness) of these eight bots were then averaged and fed back into CMA-ES to inform the parameter selection of the next generation. An optimal solution was obtained when both the design parameters and the fitness started to converge. As shown in fig. S11B, three design iterations were conducted with three different input muscle force ranges. The optimization process led to different final designs for each case, demonstrating a consistently improving speed.

Efficiency analysis through COT

The walking efficiency of the eBiobot was evaluated using COT, a dimensionless number that quantifies the energy consumption of transporting an object over a certain distance. Because it is nondimensional, this number enables a meaningful comparison against previously demonstrated biohybrid walking machines with different body scales. The COT is generally defined as

$$\mathrm{COT} = \frac{E}{mgd}$$

where E is the overall energy spent to transport a body of weight mg over the distance d. Here, we approximated the total mass of the bot as the mass of the skeleton because the masses of the muscle and electronic device (for controlling a single actuator eBiobot) are negligible. We also noted that the overall energy, including metabolic and electrical energy expenditure of the system, is hard to quantify in the case of eBiobots. We instead estimated $E \cong E_c N$, where E_c is the muscle energy output provided during each contraction and N is the number of contractions stimulated over a certain period. For consistency, the distance d is also measured over the same period of time. E_c is then quantified through the work

$$E_c = F_{act} C_{act} / 2$$

where F_{act} is the measured active force of the muscle and C_{act} is the active muscle contraction estimated from the leg deflection data recorded experimentally. We assumed that the muscle force increases linearly from rest before reaching its maximum value, hence the factor 1/2. This definition of COT did not reflect the overall energy efficiency of our system. Instead, this metric compared the efficiency of structural designs across different generations of walker bots that ultimately adopt the same walking mechanism.

Wireless control of eBiobots with console system

The multiunit dynamic control of individual eBiobots was implemented with an application-specific hardware console equipped with an Arduino Uno board. This console interfaced asynchronously via USB (universal serial bus) to the host computer that runs the GUI that communicates with the devices via NFC as described previously. Six independent controllers, which paired with six different eBiobots, produced four command events triggered by two push buttons (on+synchronous mode, on+asynchronous-left mode, on+asynchronous-right mode, and off command), which were registered with the Arduino Uno board at a refresh rate of 50 ms. These events were stored in memory until retrieved by the GUI. The GUI, at a rate of 5 s, retrieved the collection of cumulative command events from the console and stacked them in a dynamic queue for relaying them into action commands to the corresponding eBiobot on an individual basis. To account for communication errors with the eBiobots, the GUI implemented a persistent communication strategy that assured the commands were received and implemented.

Supplementary Materials

This PDF file includes:
Supplementary Methods
Figs. S1 to S30
Tables S1 to S3
References (*31*–*39*)

Other Supplementary Material for this manuscript includes the following:
Movies S1 to S16
MDAR Reproducibility Checklist

REFERENCES AND NOTES

1 A. E. Rochford, A. Carnicer-Lombarte, V. F. Curto, G. G. Malliaras, D. G. Barone, When bio meets technology: Biohybrid neural interfaces. *Adv. Mater.* **32**, 1903182 (2020).

2 J. U. Lind, T. A. Busbee, A. D. Valentine, F. S. Pasqualini, H. Yuan, M. Yadid, S.-J. Park, A. Kotikian, A. P. Nesmith, P. H. Campbell, J. J. Vlassak, J. A. Lewis, K. K. Parker, Instrumented cardiac microphysiological devices via multimaterial three-dimensional printing. *Nat. Mater.* **16**, 303–308 (2017).

3 H. Zhao, Y. Kim, H. Wang, X. Ning, C. Xu, J. Suh, M. Han, G. J. Pagan-Diaz, W. Lu, H. Li, W. Bai, O. Aydin, Y. Park, J. Wang, Y. He, M. T. A. Saif, Y. Huang, R. Bashir, J. A. Rogers, Compliant 3D frameworks instrumented with strain sensors for characterization of millimeter-scale engineered muscle tissues. *Proc. Natl. Acad. Sci. U.S.A.* **118**, e2100077118 (2021).

4 L. Riccoti, B. Trimmer, A. W. Feinberg, R. Raman, K. K. Parker, R. Bashir, M. Sitti, S. Martel, P. Dario, A. Menciassi, Biohybrid actuators for robotics: A review of devices actuated by living cells. *Sci. Robot.* **2**, eaaq0495 (2017).

5 S.-J. Park, M. Gazzola, K. S. Park, S. Park, V. di Santo, E. L. Blevins, J. U. Lind, P. H. Campbell, S. Dauth, A. K. Capulli, F. S. Pasqualini, S. Ahn, A. Cho, H. Yuan, B. M. Maoz, R. Vijaykumar, J.-W. Choi, K. Deisseroth, G. V. Lauder, L. Mahadevan, K. K. Parker, Phototactic guidance of a tissue-engineered soft-robotic ray. *Science* **353**, 158–162 (2016).

6 K. Y. Lee, S.-J. Park, D. G. Matthews, S. L. Kim, C. A. Marquez, J. F. Zimmerman, H. A. M. Ardoña, A. G. Kleberg, G. V. Lauder, K. K. Parker, An autonomously swimming biohybrid fish designed with human cardiac biophysics. *Science* **375**, 639–647 (2022).

7 O. Aydin, X. Zhang, S. Nuethong, G. J. Pagan-Diaz, R. Bashir, M. Gazzola, M. T. A. Saif, Neuromuscular actuation of biohybrid motile bots. *Proc. Natl. Acad. Sci. U.S.A.* **116**, 19841–19847 (2019).

8 R. Raman, C. Cvetkovic, S. G. M. Uzel, R. J. Platt, P. Sengupta, R. D. Kamm, R. Bashir, Optogenetic skeletal muscle-powered adaptive biological machines. *Proc. Natl. Acad. Sci. U.S.A.* **113**, 3497–3502 (2016).

9 G. J. Pagan-Diaz, X. Zhang, L. Grant, Y. Kim, O. Aydin, C. Cvetkovic, E. Ko, E. Solomon, J. Hollis, H. Kong, T. Saif, M. Gazzola, R. Bashir, Simulation and fabrication of stronger, larger, and faster walking biohybrid machines. *Adv. Funct. Mater.* **28**, 1801145 (2018).

10 J. Wang, X. Zhang, J. Park, I. Park, E. Kilicarslan, Y. Kim, Z. Dou, R. Bashir, M. Gazzola, Computationally assisted design and selection of maneuverable biological walking machines. *Adv. Intelligent Syst.* **3**, 2000237 (2021).

11 M. Guix, R. Mestre, T. Patiño, M. D. Corato, J. Fuentes, G. Zarpellon, S. Sánchez, Biohybrid soft robots with self-stimulating skeletons. *Sci. Robot.* **6**, eabe7577 (2020).

12 Z. Li, Y. Seo, O. Aydin, M. Elhebeary, R. D. Kamm, H. Kong, M. T. A. Saif, Biohybrid valveless pump-bot powered by engineered skeletal muscle. *Proc. Natl. Acad. Sci. U.S.A.* **116**, 1543–1548 (2019).

13 Y. Morimoto, H. Onoe, S. Takeuchi, Biohybrid robot powered by an antagonistic pair of skeletal muscle tissues. *Sci. Robot.* **3**, eaat4440 (2018).

14 S. R. Shin, B. Migliori, B. Miccoli, Y.-C. Li, P. Mostafalu, J. Seo, S. Mandla, A. Enrico, S. Antona, R. Sabarish, T. Zheng, L. Pirrami, K. Zhang, Y. S. Zhang, K.-T. Wan, D. Demarchi, M. R. Dokmeci, A. Khademhosseini, Electrically driven microengineered bio-inspired soft robots. *Adv. Mater.* **30**, 1704189 (2018).

15 V. Chan, K. Park, M. B. Collens, H. Kong, T. A. Saif, R. Bashir, Development of miniaturized walking biological machines. *Sci. Rep.* **2**, 857 (2012).

16 H. A. Ledesma, X. Li, J. L. Carvalho-de-Souza, W. Wei, F. Bezanilla, B. Tian, An atlas of nano-enabled neural interfaces. *Nat. Nanotechnol.* **14**, 645–657 (2019).

17 Y. Yang, M. Wu, A. Vázquez-Guardado, A. J. Wegener, J. G. Grajales-Reyes, Y. Deng, T. Wang, R. Avila, J. A. Moreno, S. Minkowicz, V. Dumrongprechachan, J. Lee, S. Zhang, A. A. Legaria, Y. Ma, S. Mehta, D. Franklin, L. Hartman, W. Bai, M. Han, H. Zhao, W. Lu, Y. Yu, X. Sheng, A. Banks, X. Yu, Z. R. Donaldson, R. W. Gereau, C. H. G. IV, Z. Xie, Y. Huang, Y. Kozorovitskiy, J. A. Rogers, Wireless multilateral devices for optogenetic studies of individual and social behaviors. *Nat. Neurosci.* **24**, 1035–1045 (2021).

18 A. D. Mickle, S. M. Won, K. N. Noh, J. Yoon, K. W. Meacham, Y. Xue, L. A. Mcilvried, B. A. Copits, V. K. Samineni, K. E. Crawford, D. H. Kim, P. Srivastava, B. H. Kim, S. Min, Y. Shiuan, Y. Yun, M. A. Payne, J. Zhang, H. Jang, Y. Li, H. H. Lai, Y. Huang, S.-I. Park, R. W. Gereau IV, J. A. Rogers, A wireless closed-loop system for optogenetic peripheral neuromodulation. *Nature* **565**, 361–365 (2019).

19 A. Vázquez-Guardado, Y. Yang, A. J. Bandodkar, J. A. Rogers, Recent advances in neurotechnologies with broad potential for neuroscience research. *Nat. Neurosci.* **23**, 1522–1536 (2020).

20 Y. Liu, J. Li, S. Song, J. Kang, Y. Tsao, S. Chen, V. Mottini, K. McConnell, W. Xu, Y.-Q. Zheng, J. B.-H. Tok, P. M. George, Z. Bao, Morphing electronics enable neuromodulation in growing tissue. *Nature* **38**, 1031–1036 (2020).

21 G. Shin, A. M. Gomez, R. Al-Hasani, Y. R. Jeong, J. Kim, Z. Xie, A. Banks, S. M. Lee, S. Y. Han, C. J. Yoo, J.-L. Lee, S. H. Lee, J. Kurniawan, J. Tureb, Z. Guo, J. Yoon, S.-I. Park, S. Y. Bang, Y. Nam, M. C. Walicki, V. K. Samineni, A. D. Mickle, K. Lee, S. Y. Heo, J. G. McCall, T. Pan, L. Wang, X. Feng, T.-I. Kim, J. K. Kim, Y. Li, Y. Huang, R. W. Gereau IV, J. S. Ha, M. R. Bruchas, J. A. Rogers, Flexible near-field wireless optoelectronics as subdermal implants for broad applications in optogenetics. *Neuron* **93**, 509–521 (2017).

22 M. Gazzola, L. H. Dudte, A. G. McCormick, L. Mahadevan, Forward and inverse problems in the mechanics of soft filaments. *R. Soc. Open Sci.* **5**, 171528 (2018).

23 X. Zhang, F. K. Chan, T. Parthasarathy, M. Gazzola, Modeling and simulation of complex dynamic musculoskeletal architectures. *Nat. Comm.* **10**, 4825 (2019).

24 N. Hansen, "The CMA evolution strategy: A comparing review," in *Towards a New Evolutionary Computation* (Springer, Berlin, 2006), pp. 75–102.

25 C. Cvetkovic, M. C. Ferrall-Fairbanks, E. Ko, L. Grant, H. Kong, M. O. Platt, R. Bashir, Investigating the life expectancy and proteolytic degradation of engineered skeletal muscle biological machines. *Sci. Rep.* **7**, 3775 (2017).

26 J. Wang, Y. Wang, Y. Kim, T. Yu, R. Bashir, Multi-actuator light-controlled biological robots. *APL Bioeng.* **6**, 036103 (2022).

27 T. Tominaga, N. Takedomi, H. Biederman, H. Furukawa, Y. Osada, J. P. Gong, Effect of substrate adhesion and hydrophobicity on hydrogel friction. *Soft Matter* **4**, 1033–1040 (2008).

28 R. Raman, C. Cvetkovic, R. Bashir, A modular approach to the design, fabrication, and characterization of muscle-powered biological machines. *Nat. Prot.* **12**, 519–533 (2017).

29 C. Cvetkovic, R. Raman, V. Chan, B. J. Williams, M. Tolish, P. Bajaj, M. S. Sakar, H. H. Asada, M. T. A. Saif, R. Bashir, Three-dimensionally printed biological machines powered by skeletal muscle. *Proc. Natl. Acad. Sci. U.S.A.* **111**, 10125–10130 (2014).

30 T. Bruegmann, T. van Bremen, C. C. Vogt, T. Send, B. K. Fleischmann, P. Sasse, Optogenetic control of contractile function in skeletal muscle. *Nat. Comm.* **6**, 7153 (2015).

31 V. T. Hoang, G. Stępniewski, K. H. Czarnecka, R. Kasztelanic, V. C. Long, K. D. Xuan, L. Shao, M. Śmietana, R. Buczyński, Optical properties of buffers and cell culture media for optofluidic and sensing applications. *Appl. Sci.* **9**, 1145 (2019).

32 C. W. J. Oomens, M. Maenhout, C. H. van Oijen, M. R. Drost, F. P. Baaijens, Finite element modelling of contracting skeletal muscle. *Philos. Trans. R. Soc. Lond., B, Biol. Sci.* **358**, 1453–1460 (2003).

33 A. W. Feinberg, A. Feigel, S. S. Shevkoplyas, S. Sheehy, G. M. Whitesides, K. K. Parker, Muscular thin films for building actuators and powering devices. *Science* **317**, 1366–1370 (2007).

34 J. C. Nawroth, H. Lee, A. W. Feinberg, C. M. Ripplinger, M. L. McCain, A. Grosberg, J. O. Dabiri, K. K. Parker, A tissue-engineered jellyfish with biomimetic propulsion. *Nat. Biotechnol.* **30**, 792–797 (2012).

35 B. J. Williams, S. V. Anand, J. Rajagopalan, M. T. A. Saif, A self-propelled biohybrid swimmer at low Reynolds number. *Nat. Comm.* **5**, 3081 (2014).

36 J. Xi, J. J. Schmidt, C. D. Montemagno, Self-assembled microdevices driven by muscle. *Nat. Mater.* **4**, 180–184 (2005).

37 J. Kim, J. Park, S. Yang, J. Baek, B. Kim, S. H. Lee, E.-S. Yoon, K. Chun, S. Park, Establishment of a fabrication method for a long-term actuated hybrid cell robot. *Lab. Chip* **7**, 1504–1508 (2007).

38 B. C. W. Kot, Z. J. Zhang, A. W. C. Lee, V. Y. F. Leung, S. N. Fu, Elastic modulus of muscle and tendon with shear wave ultrasound elastography: Variations with different technical settings. *PLOS ONE* **7**, e44348 (2012).

39 J. Mendez, A. Keys, Density and composition of mammalian muscle. *Metab. Clin. Exp.* **9**, 184–188 (1960).

Acknowledgments

We thank R. Kamm from Massachusetts Institute of Technology for providing the transfected cell line used in this study, the staff at the Holonyak Micro and Nanotechnology Laboratory at UIUC, and J. Yo, M. Wester, and Y. Jeong for editing videos and illustrations. This research used the Micro/Nano Fabrication Facility at Northwestern University, the Holonyak Micro and Nanotechnology Laboratory, and the Extreme Science and Engineering Discovery Environment (XSEDE). The content is solely the responsibility of the authors and does not necessarily represent the official views of National Institutes of Health (NIH). **Funding:** This work was funded by NSF Emerging Frontiers in Research and Innovation C3 SoRo Grant 1830881 (to M.G. and R.B.); NSF Research Traineeship-Miniature Brain Machinery Grant 173525 (to R.B.); NSF Science and Technology Center Emergent Behavior of Integrated Cellular Systems Grant CBET0939511 (to R.B.); the Querrey Simpson Institute for Bioelectronics, Northwestern University (JAR); NSF Soft and Hybrid Nanotechnology Experimental Resource ECCS-1542205 (to J.A.R.); National Institute of Biomedical Imaging and Bioengineering of the NIH Award T32EB019944 (to Y.K.); NSF Expeditions in Computing Grant 2123781 (to M.G.); and NSF Grant for XSEDE ACI-1548253, through allocation TG-MCB190004 (to M.G.). **Author contributions:** Conceptualization and design: Y.K., Y.Y., X.Z., Z.L., A.V.-G., M.G., J.A.R., and R.B. Electronic fabrications and characterizations: Y.Y., Z.L., A.V.-G., A.I.E., Y.W., H.L., X.N., J.J.P., Z.X., and H.Z. Biofabrication and analysis for eBiobots: Y.K., I.P., J.W., Y.S.K., and J.B. Computational modeling and design: X.Z., Z.D., and J.P. Writing: Y.K., Y.Y., X.Z., Z.L., A.V.-G., I.P., M.G., J.A.R., and R.B. **Competing interests:** The authors declare that they have no competing interests. **Data and materials availability:** All data are available in the main text or the Supplementary Materials. Computational modeling was performed using numerical solver Elastica, which is publicly available at www.cosseratrods.org. Code and scripts associated with the hardware manipulation to control the devices wirelessly are available upon request.

Submitted 20 May 2022
Accepted 21 December 2022
Published 18 January 2023
10.1126/scirobotics.add1053

Science Robotics

Remote control of muscle-driven miniature robots with battery-free wireless optoelectronics

Yongdeok Kim, Yiyuan Yang, Xiaotian Zhang, Zhengwei Li, Abraham Vzquez-Guardado, Insu Park, Jiaojiao Wang, Andrew I. Efimov, Zhi Dou, Yue Wang, Junehu Park, Haiwen Luan, Xinchen Ni, Yun Seong Kim, Janice Baek, Joshua Jaehyung Park, Zhaoqian Xie, Hangbo Zhao, Mattia Gazzola, John A. Rogers, and Rashid Bashir

Sci. Robot., **8** (74), eadd1053.
DOI: 10.1126/scirobotics.add1053